JOURNAL OF SPACECRAFT AND ROCKETS
Vol. 47, No. 5, September–October 2010

Radiation Modeling for the Reentry of the Stardust Sample Return Capsule

Yen Liu*
NASA Ames Research Center, Moffett Field, California 94035
Dinesh Prabhu†
ELORET Corporation, Sunnyvale, California 94086
Kerry A. Trumble‡
NASA Ames Research Center, Moffett Field, California 94035
David Saunders§
ELORET Corporation, Sunnyvale, California 94086
and
Peter Jenniskens¶
SETI Institute, Mountain View, California 94043

DOI: 10.2514/1.37813

A high-fidelity three-dimensional approach is developed to simulate emission signatures from the shock layer around the Stardust sample return capsule at several points on its best-estimated trajectory. Calculations are performed with various gas chemistry, thermodynamic, and radiation models. Results are compared against calibrated imaging data acquired by a slitless echelle spectrometer. The present analysis is based on flowfields computed without the inclusion of ablation products, and the comparison is focused on radiation from atomic oxygen and nitrogen lines. The purpose is to apply and improve, if necessary, the current models used in nonequilibrium atmospheric entry simulations.

I. Introduction

THE Stardust spacecraft, launched in February 1999, was part of a mission to collect comet dust samples during its encounter with comet Wild 2 and to gather samples of interstellar dust. Analysis of these celestial grains could help lead us to understand the evolution of the sun and its planets and, possibly, even the origin of life. These samples were brought back to Earth from interplanetary space by a sample return capsule (SRC) in January 2006. The SRC, with a 60 deg sphere–cone heat shield and (truncated) conical backshell (see Fig. 1), was roughly 0.8 m in diameter and entered Earth's atmosphere at a speed of 12.8 km/s, the fastest man-made object ever to traverse our atmosphere. The spacecraft thermal protection system (TPS) was not instrumented to gather flight-based material performance data, which would have been very valuable in the future design of heat shields for spacecraft entering Earth's atmosphere at hyperbolic orbital speeds. Fortunately, however, the reentry event was observed by a team of researchers aboard NASA's DC-8 Airborne Observatory. Imaging and spectroscopic data were acquired for a period of 60 s, starting at approximately 6 s after atmospheric entry. The measurement period was roughly centered around the peak of the heating pulse. Radiative signals from the shock layer surrounding the SRC were measured by eight different instruments with various spectral and temporal resolutions. The SRC approached too far from the cameras to be resolved: the capsule appears on the instruments as a single pixel. Nevertheless, these Stardust SRC entry observations provide a rare and highly detailed spectral data set of interplanetary speed entry shock-generated radiation.

The TPS of the SRC was made of an ablative material known as PICA (phenolic-impregnated carbon ablator), developed at NASA Ames Research Center. Methods of computational fluid dynamics (CFD) were extensively used to define the design-to aerothermal environments for the heat shield. For instance, Olynick et al. [1] applied a continuum Navier–Stokes flow solver, loosely coupled to radiation and material thermal response models, to predict Stardust SRC entry aerothermal environments for altitudes from 80 down to 43 km. In a more recent analysis of Stardust entry environments, mostly for verification of adequacy of TPS design margins, Park [2] used viscous shock-layer analysis to predict heating rates for the Stardust capsule along a portion of a candidate flight trajectory for altitudes ranging from 76 down to about 46 km. The finding from the various studies was that the aerothermal environments around the spacecraft had only a small contribution from shock-layer radiation, owing to the small size of the configuration, despite the extremely high-entry velocity. Convective heating dominated the aerothermal environments.

The entry observations, together with the recovered capsule, provided an opportunity to determine the accuracy of the predictive tools used in the design. One approach toward verification/validation of predictive tools would be to use them to determine heating environments along the trajectory reconstructed from flight observations (i.e., the best-estimated trajectory, or BET [3,4]), use these environments to determine material thermal response (mass loss due to a combination of ablation and recession), and compare predictions against onground measurements of the recovered capsule. Another approach would be to apply the predictive tools to construct the shock-layer emission profile along the BET and compare the results against the spectral/temporal measurements from the instrument suite used in the entry imaging campaign. The latter approach is the focus of the present work.

In this work, a high-fidelity three-dimensional methodology was developed to simulate the SRC shock-layer emission signatures at

Presented as Paper 2008-1213 at the 46th AIAA Aerospace Sciences Meeting and Exhibit, Reno, NV, 7–10 January 2008; received 31 March 2008; revision received 23 May 2009; accepted for publication 28 March 2010.

*Research Scientist; yen.liu@nasa.gov.
†Senior Research Scientist. Associate Fellow AIAA.
‡Research Scientist. Member AIAA.
§Senior Research Scientist. Member AIAA.
¶Astronomer, Principal Investigator, Carl Sagan Center, 515 N. Whisman Road. Member AIAA.

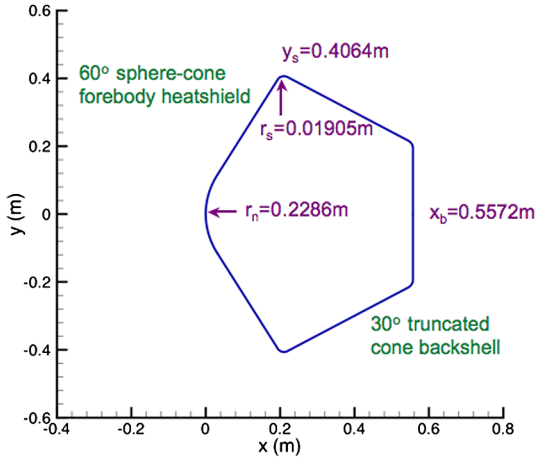

Fig. 1 Stardust SRC surface geometry.

several points along the BET. Emission computations were performed using NEQAIR [5], a spectral line-by-line radiation code with one-dimensional energy transport. Assuming the shock layer to be adiabatic (i.e., spatial divergence of the radiative heat flux is not included in the flow energy conservation equation), NEQAIR is applied a posteriori to precomputed flowfields to determine radiative intensities emerging from the shock layer. The requisite thermochemical quantities (temperatures and species number densities) of the shock layer were extracted from flowfields computed using a state-of-the-art thermochemical nonequilibrium flow solver, DPLR (data parallel line relaxation) [6]. The simplifying first step taken was to focus on emission from the shock layer without the presence of any products of material ablation. It is then sufficient to work with flowfields that have been computed with either an 11- or 12-species air model (argon being the 12th species). To establish a baseline for signatures of carbon-bearing species (specifically CN) due to the presence of atmospheric carbon dioxide, emission computations are also performed using flowfields computed with a 17-species air model. Since the methodology simulates emission intensities emerging from the shock layer, as an initial-value problem, it requires the specification of intensity to integrate the radiation transport equation. In the present work, this initial intensity is that of a blackbody radiating at the surface radiation equilibrium temperature (albeit, without any heat conduction through the material) computed as part of the flowfield. For all of the radiation simulations, calibrated data acquired by the echelle spectrograph [7] used in the SRC entry imaging campaign are the basis for comparisons.

II. Flow and Radiation Modeling

There are three approaches one could take for computing the thermal radiation generated from the shock layer around a high-speed entry vehicle:

1) A fully coupled approach in which the flow equations and the radiative transfer equation (RTE) are solved simultaneously. Because of the frequency and angular dependence of the radiative specific intensity, this approach is prohibitively expensive, especially for a full three-dimensional problem. However, the use of some restrictive assumptions about the frequency and angular dependence can make this approach more tractable [8,9].

2) An uncoupled approach in which the flow equations are solved first without consideration of radiation, and the RTE is then solved using the temperature(s) and species' number densities obtained from a converged flowfield solution. This approach provides a fast turnaround time for computing the radiative heating. Thus, the frequency and angular dependence of the specific intensity can be handled more accurately with a spectroscopic line-by-line basis and a full angular integration. In addition, the radiative heat flux estimates are conservative.

3) A loosely coupled approach in which the uncoupled approach is applied first, then the flow equations are integrated again using the newly computed divergence of the radiative heat flux from the solution of the RTE. This cycle is repeated until both flow and radiation fields converge. While being simpler to implement than the fully coupled approach, this iterative process might be numerically sensitive or, sometimes, even nonconvergent.

In the current study, in order to handle the frequency and angular dependence of the specific intensity with better accuracy, we adopt the uncoupled approach. All flowfield solutions are carried out using the DPLR code, and radiation simulations are performed by the NEQAIR radiation code. DPLR is a parallel, multiblock finite-volume code that solves the full set of Navier–Stokes equations, including the effects of finite-rate chemistry and thermal nonequilibrium. Inviscid fluxes are computed using a modified Steger–Warming flux splitting. The spatial accuracy up to the third order is obtained through MUSCL extrapolation coupled with a minmod flux limiter. Viscous fluxes are computed with a second-order central difference scheme. Transport properties are based on accurate collision integrals [10,11] with Gupta et al. mixing rules [12]. Diffusion coefficients are calculated using either of two models: 1) the bifurcation model [13] (baseline model for all flowfield computations), or 2) the self-consistent effective binary diffusion model [14]. The data-parallel line relaxation method is employed for implicit time advancement to a steady-state solution. In all our calculations, the flow is assumed laminar; the surface is flux-limited fully catalytic and is in radiative equilibrium, with an emissivity value of 0.85. It should be noted that the flowfield computations do not include material response. Hence, the predicted radiation equilibrium temperatures are expected to be higher than those that would be obtained if material response (heat conduction and ablation) were included in the analysis. NEQAIR is a serial computer code that solves the specific intensity by directly integrating the RTE along a line of sight (LOS), using a first-order quadrature. In calculating the radiative heat flux on the body surface, NEQAIR assumes the flow to vary one-dimensionally in the direction normal to the body and employs the tangent-slab approximation for the angular integration. This greatly simplifies the treatment of radiation transport, thereby allowing the frequency dependence to be treated in more detail, line-by-line, spectroscopically. In the following, we discuss the modeling of the gas chemistry, thermodynamics, and radiation used in our simulations.

A. Gas Chemistry

The present analysis is based on nonablating simulation. We consider only the air species and reactions at high temperatures. Here, we adopt the Park 1990 model [15] (Park90) as our baseline for the gas chemistry. This is an 11-species and 19-reactions finite-rate air model (denoted by 11) consisting of N_2, O_2, NO, N_2^+, O_2^+, NO^+, N, O, N^+, O^+, and e^-. To establish a baseline of CN radiation from the small amount (roughly 0.05% by volume) of CO_2 in the Earth atmosphere, and to prepare for a future study of ablation, we also employ a 17-species and 33-reactions air model (denoted by 17) with CO_2, CN, CO, C_2, C, and Ar as additional species. The reaction rates are taken from Park et al. [16] (Park94). In addition, a 12-species and 22-reactions air model (denoted by 12) is also used to study the influence of Ar on radiative heating. Three dissociation reactions involving N_2, O_2, and NO with Ar are added to the Park90 model, and the reaction rates from Gessman et al. [17] are used here. The freestream compositions (mass fractions) for each model are listed in Table 1.

Table 1 Freestream compositions (mass fractions) of chemistry models

Chemistry model	Air11	Air12	Air17
N_2	0.767000	0.755481	0.755197
O_2	0.233000	0.231694	0.231425
Ar	——	0.012825	0.012891
CO_2	——	——	0.000487

B. Gas Thermodynamics

The Park90 and Park94 reaction rates were determined or compiled without taking into consideration excited electronic states of atoms and molecules. Therefore, the baseline thermodynamic model (denoted by G) assumes all species to be in their ground electronic states. In addition, diatomic molecules are assumed to be rigid rotor/simple harmonic oscillators for their rotational–vibrational states. Note that neglecting excited electronic states may result in too-high temperatures and, thus, inaccurate reaction rates. Furthermore, there would be no radiation if all atoms were in their ground electronic states. We therefore also investigate a variant model (denoted by E) that includes contributions of excited electronic states to partition functions for all species. Since reaction rates involving excited electronic states are currently unavailable, the baseline rates are also used for the variant model. Both models employ multiple temperatures to describe thermal nonequilibrium. The translational temperature for all species is assumed to be the same. For the case of molecular species, the rotational temperature is assumed to be fully equilibrated with the translational temperature (i.e., $T_{\text{rot}} = T_{\text{tran}} = T$). Also, the vibrational and electronic temperatures are assumed to be the same (i.e., $T_{\text{vib}} = T_{\text{elec}} = T_v$), and the free electron temperature is assumed to be the same as the mixture translational temperature (i.e., $T_e = T$). For dissociation reactions, the geometric average of the translational and vibration temperatures, $T_{\text{avg}} = \sqrt{TT_v}$, is used to determine the rates. The energy exchange between the translational-rotational and vibration-electronic modes is modeled by the Landau–Teller formulation. Vibrational relaxation times are obtained from Millikan and White [18], assuming simple harmonic oscillators, with the high-temperature correction of Park [15].

C. Energy State Populations

The problem of calculating radiative transport through the shock layer is solved by direct integration of the RTE. The source function and absorption coefficient in the RTE are determined by the temperatures (T and T_v) and populations of the transition energy states. The computed number densities N_s from the flow solution have to be distributed among the various energy states of the constituent atoms and molecules. Our baseline radiation model is based on the quasi-steady state (QSS) assumption (denoted by Q) [15] in which rate processes governed by electron impact determine populations of select states. The QSS model has been calibrated for the 11-species air model and was able to replicate a shock-tube experiment and the spectro-/radiometric data from the Fire II flight experiment [19]. However, those rates for carbon-bearing species have not been determined yet. Therefore, for the 17-species air model, we use the Boltzmann distribution (denoted by B) to determine the populations of the various energy states. To study the effect of changing the radiation models, both the QSS and Boltzmann models are used for the 12-species air calculations.

D. Spectral Lines and Bands

There are a large number of electronic states of atoms and molecules that can be considered in detailed line-by-line spectroscopic computations. The specific line and band systems chosen for the present work are shown in Table 2. Most of the important molecular band systems in the wavelength (λ) range of 80 to 1,400 nm are included in the analysis. This wide wavelength range is divided into 218 subregions of varying lengths, 2.5 nm in the wavelength range of 80 to 100 nm, 5.0 nm in the wavelength range from 100 to 900 nm, and 10.0 nm in the wavelength range from 900 to 1400 nm. Each subregion is further divided into 50,000 fine intervals. This distribution of wavelength intervals gives a very fine resolution, over 10 million spectral points, in the wavelength (or frequency) variable of the RTE.

Table 2 Line and band systems for radiative heating computations using NEQAIR

Species	Systems
N	Lines/multiplets between 80 and 1400 nm
O	Lines/multiplets between 80 and 1400 nm
N^+, O^+, e^-	Bound–free and free–free continua
N_2	1st positive ($B^3\Pi_g \rightarrow A^3\Sigma_u^+$), 2nd positive ($C^3\Pi_u \rightarrow B^3\Pi_g$)
O_2	Schumann–Runge ($B^3\Sigma_u^- \rightarrow X^3\Sigma_g^-$)
NO	$\beta(B^2\Pi \rightarrow X^2\Pi)$ and $\gamma(A^2\Sigma^- \rightarrow X^2\Pi)$
N_2^+	1st negative ($B^2\Sigma_u^+ \rightarrow X^2\Sigma_g^+$)
C	Lines/multiplets between 80 and 1400 nm
CN	Violet ($B^2\Sigma^+ \rightarrow X^2\Sigma^+$, Red ($A^2\Pi \rightarrow X^2\Sigma^+$)
CO	4th positive ($A^1\Pi \rightarrow X^1\Sigma^+$)

E. Angular Integration

In the angular part of the integration for solving the RTE, we employed both the tangent-slab approximation and a full angular integration. While the former is used for computing the radiative heat flux to the body surface (inward calculation), the latter is applied for computing the specific flux density (flux per unit wave length) to the observer (outward calculation) to compare with the observation data. The tangent-slab approximation is a very common practice for estimating the level of radiative heat flux to the body surface. In this approach, lines of sight normal to the surface are integrated from the shock to the body. The Stardust SRC aeroshell consists of two primary components: a 60 deg sphere–cone forebody heat shield with a nose radius of 0.2286 m and a shoulder radius of 0.01905 m and a 30 deg truncated cone backshell. The width at maximum diameter is 0.8128 m, and the length is 0.5572 m. Figure 1 shows its surface geometry, and Fig. 2 depicts the normal direction lines of sight. Although this approximation simplifies the radiative transport to one dimension, it has been shown to produce good results around the peak-heating region [20].

The situation is different for computing radiation toward the observer. Although the radiative signal toward the observer appears on the instruments as a single pixel, the instruments actually collect all signals emitted from the entire body surface of the SRC and the surrounding shock-layer gases. Because the shock-layer flowfield and SRC body temperature are very nonuniform, we have a very nonuniform emitting source field. Furthermore, since the viewing direction is not along the flow axis of symmetry, the radiation field becomes truly three-dimensional. The lines of sight are no longer exclusively in the symmetry plane. Because of the strong nonlinearity between the specific intensity and the temperatures and species number densities, using a single line of sight with some kind of averaging would not provide an accurate radiation field. To account for this, we developed a three-dimensional procedure for the angular integration to sum all the signals emitted to the instruments. A schematic sketch of the problem is shown in Fig. 3. First, the axisymmetric DPLR solution was replicated circumferentially to create a three-dimensional flowfield. We next determined the view angle and the distance from the observer to the SRC, using the BET

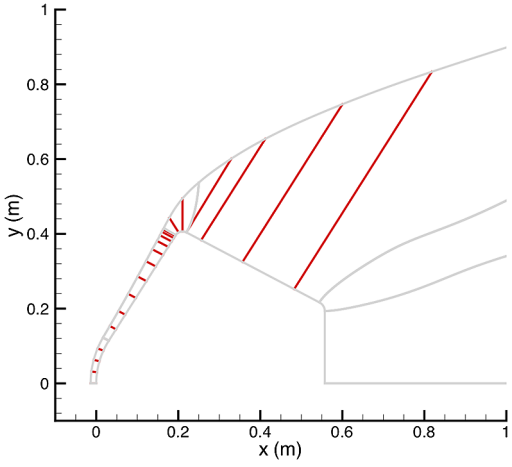

Fig. 2 Normal direction lines of sight.

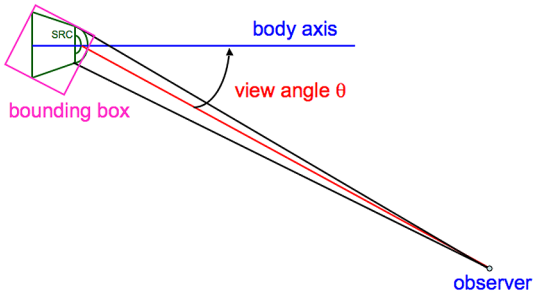

Fig. 3 Schematic sketch.

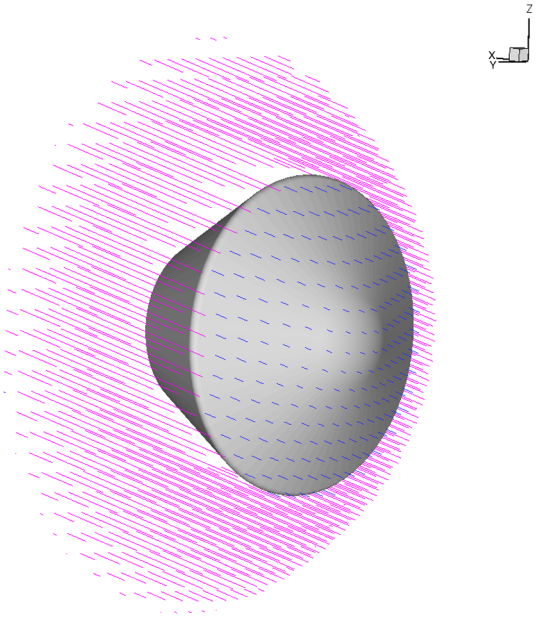

Fig. 4 Lines of sight for the full angular integration.

[3,4]. Based on the view angle, we created a bounding boxcovering the flowfield, with the front and back planes of the box perpendicular to the viewing direction. We used a uniform Cartesian grid on the back plane to construct lines of sight that emanated from the body surface and shock layer to the outer domain of the flowfield in the direction to the observer. In Fig. 4, we show these lines of sight from both the body surface and the shock layer. On each line of sight, the temperatures and species number densities were obtained by interpolations from the three-dimensional flow solution. NEQAIR was then used to integrate the RTE for each line of sight. Since a uniform angular grid was used, the total emission was obtained by summing the solutions of all lines of sight and multiplying by the solid angle of a single grid cell.

III. Numerical Results

In the postflight analysis, the as-flown trajectory of the Stardust SRC was determined and found to be very similar to the last predicted reentry trajectory. Based on the in-space navigation, airborne observation, ground photos, and terminal decent radar, Desai et al. [3] and Levit et al. [4] have reconstructed the SRC reentry trajectory. In addition, the relative distances and view angles from the DC-8 airborne observatory to the SRC were also determined. This reconstructed trajectory provides the best flight conditions, including the altitudes and freestream conditions, for the postflight flow and radiation analyses. The Stardust SRC entered the Earth atmosphere at a coordinated universal time of 09:56:42.28 on 15 January 2006. In this paper, we use this entry time as the reference time $t = 0$ s; all other time is measured from this time. Our calculations started at time $t = 34$ s (altitude $z = 81.02$ km) and ended at $t = 66$ s

Table 3 Freestream conditions and relative observer positions at various trajectory points

t (from entry)	34	36	38	40	42	44	46	48	51	53	56	59	62	66
z, km	81.02	78.46	75.96	73.54	71.19	68.93	66.76	64.69	61.76	59.95	57.46	55.23	53.25	50.98
V, m/s	12385.12	12336.86	12269.13	12181.08	12062.73	11902.13	11689.11	11414.01	10871.38	10417.96	9617.36	8708.65	7751.20	6504.45
ρ, kg/m^3	1.2690E-05	1.8710E-05	2.7240E-05	3.9220E-05	5.5520E-05	7.7220E-05	1.0531E-04	1.4099E-04	2.1100E-04	2.6964E-04	3.7506E-04	4.9983E-04	6.4261E-04	8.5435E-04
T, K	217.63	218.09	218.69	219.96	221.82	224.14	227.56	230.79	234.95	237.68	243.10	248.00	251.70	255.84
Distance, km	419.51	395.27	371.17	347.25	323.59	300.27	277.39	255.09	223.04	202.87	174.88	149.74	128.14	104.68
View angle, deg	10.73	11.27	11.90	12.60	13.41	14.33	15.40	16.62	18.85	20.61	23.81	27.76	32.52	40.41

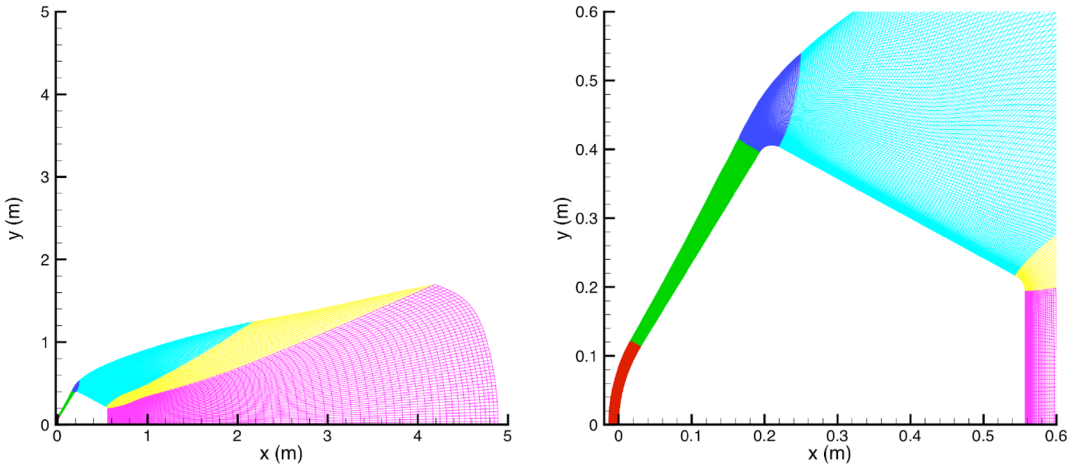

a) Complete b) Near SRC

Fig. 5 Computational grid.

($z = 50.98$ km), with a total of 14 points along the reconstructed trajectory. The peak heating occurred at $t = 51$ s ($z = 61.76$ km). Table 3 shows the freestream conditions together with the distances and view angles from the observer to the SRC at these points. Continuum flow was assumed throughout. Note that, based on the Knudsen number and the breakdown parameter [21], at the altitude $z = 81.02$ km, the flow is on the border of being noncontinuum, and the validity of our predictions may be questionable at this high altitude.

A. Flowfields

As described above, the DPLR code was used for the flow simulations. The reentry trajectory for the SRC was designed to be

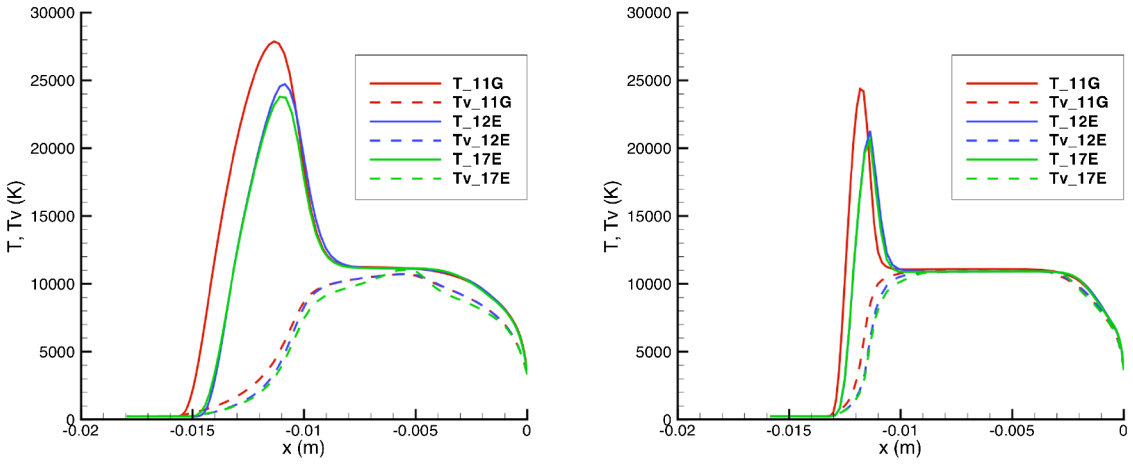

a) t = 42s b) t = 51s

Fig. 6 Stagnation line translational and vibrational temperature distribution.

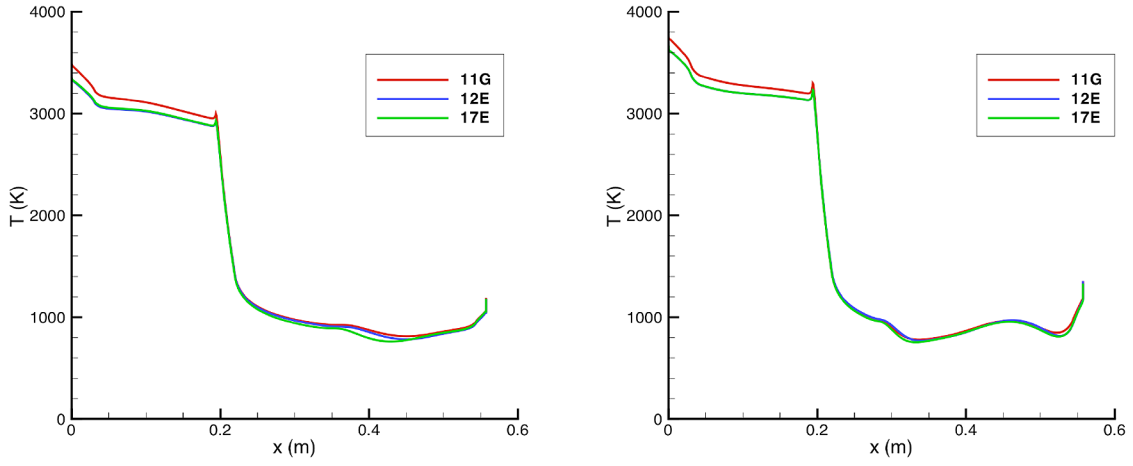

a) t = 42s b) t = 51s

Fig. 7 Body surface translational and vibrational temperature distribution.

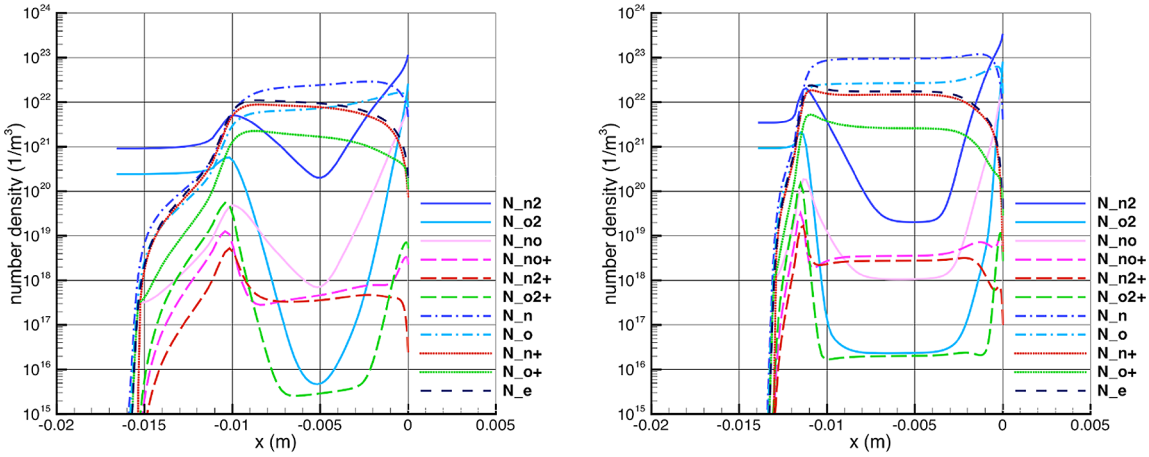

a) t = 42s **b) t = 51s**

Fig. 8 Stagnation line species number density distribution using model 11G.

purely ballistic; therefore, the nominal angle of attack was 0 deg. Two-dimensional axisymmetric flow solutions using the baseline model, 11-species ground state thermodynamics (11G), and the alternative model 12-species excited-state thermodynamics (12E) were calculated for the 14 trajectory points. For the purpose of comparing radiative heating, the 17-species excited thermodynamics (17E) model was also used to obtain results at $t = 42$ s and $t = 51$ s. Since this paper deals with the radiation modeling, here, we only show the results for temperatures and species number densities at $t = 42$ s and $t = 51$ s. All calculations were carried out on a grid consisting of six zones and a total of 342×129 points. The grid is shown in Fig. 5a, and the part around the body is plotted in Fig. 5b.

In Figs. 6a and 6b, we show the translational and vibrational temperature distributions along the stagnation line at the two

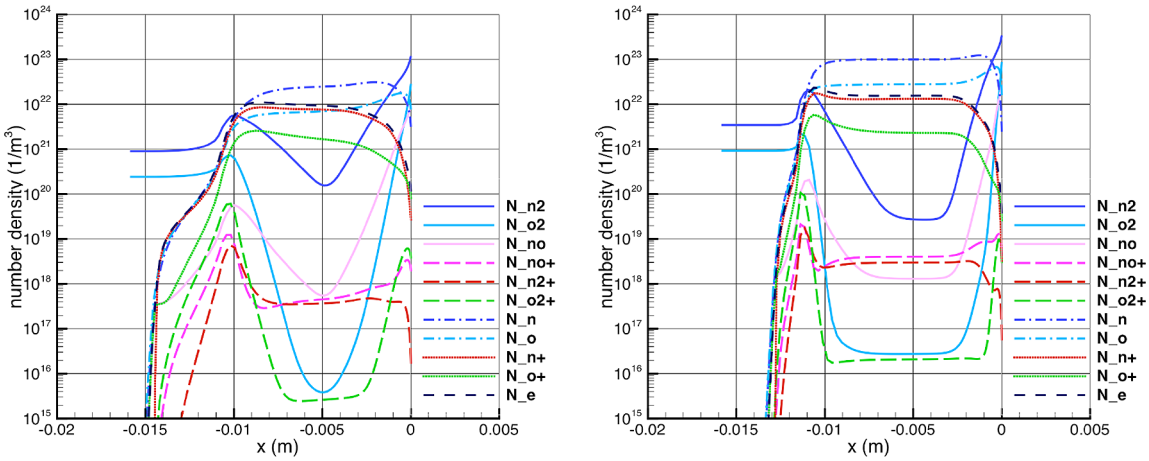

a) t = 42s **b) t = 51s**

Fig. 9 Stagnation line species number density distribution using model 12E.

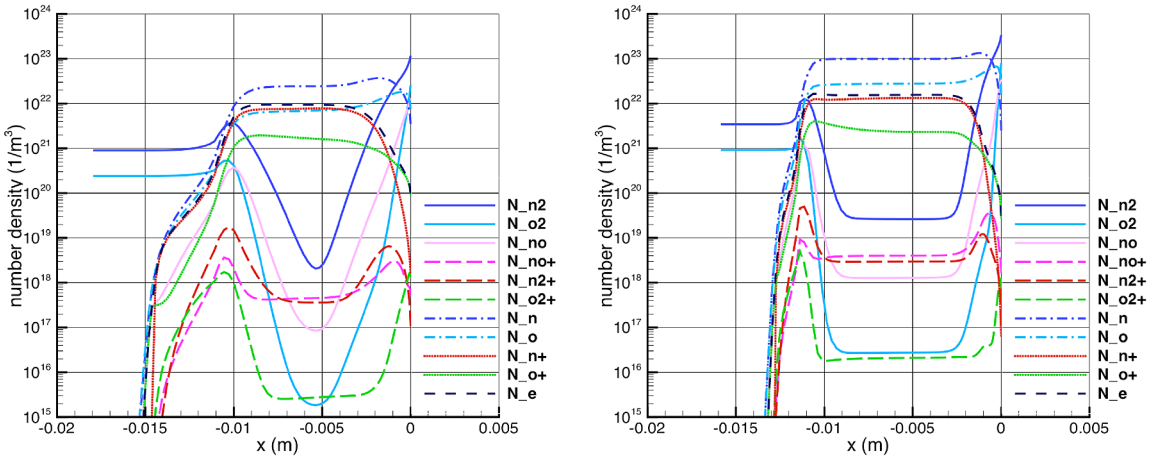

a) t = 42s **b) t = 51s**

Fig. 10 Stagnation line species number density distribution using model 17E.

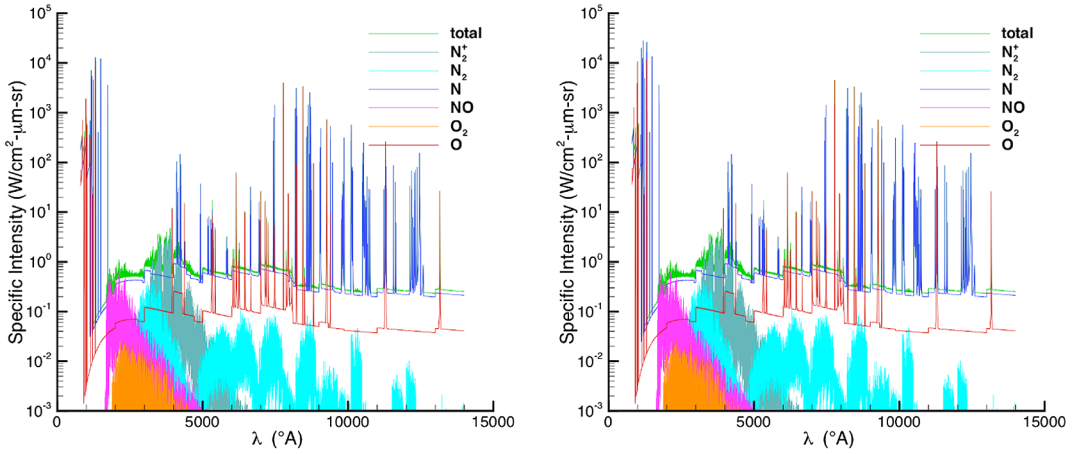

a) Inward **b) Outward**

Fig. 11 Stagnation point specific intensity spectra by species using model 11GQ (log scale).

trajectory points. Among the three models, the shock-layer temperature using the ground state thermodynamics model (G) is hotter than that using the excited-state thermodynamics models (E). This is because the latter allows part of the energy to be stored in the internal excited modes. Between the two excited-state thermodynamics models, the 12-species one has a slightly higher temperature profile than the 17-species one.

The Stardust SRC is a rather small blunt body with a maximum diameter of 0.8 m (cf., 5 m for the current Orion Command Module configuration). The shock standoff distances are extremely small, approximately 1.3–1.5 cm at $t = 42$ s and 1.2–1.3 cm at $t = 51$ s. This results in a very high convective heat flux to the body, more than 90% of the total heat flux. The radiative heat flux accounts for less than 10% of the total heat flux. Comparing the translational and

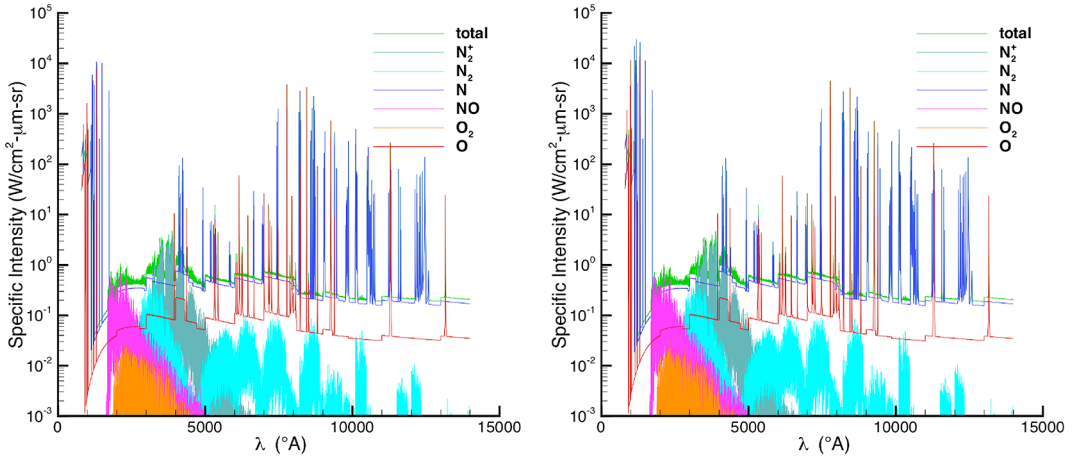

a) Inward **b) Outward**

Fig. 12 Stagnation point specific intensity spectra by species using model 12EQ (logarithmic scale).

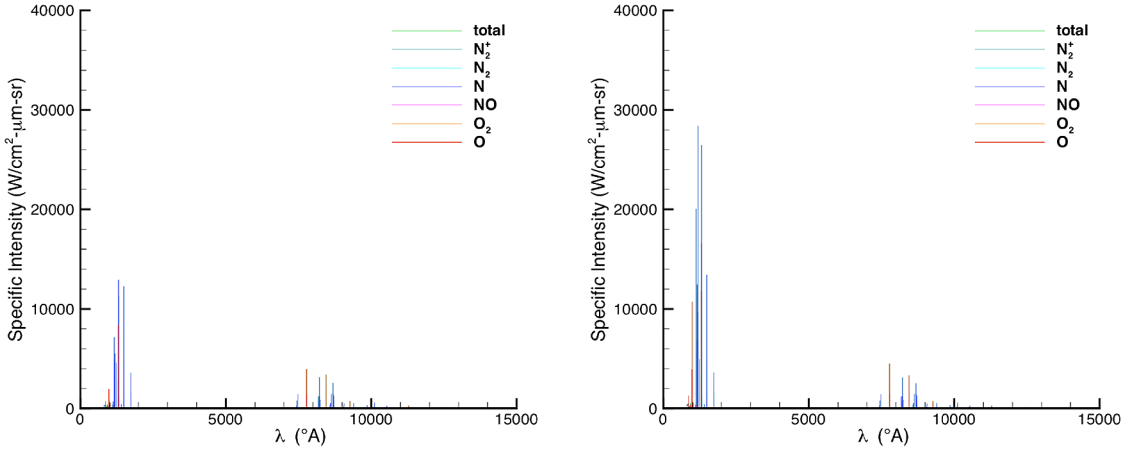

a) Inward **b) Outward**

Fig. 13 Stagnation point specific intensity spectra by species using model 11GQ (linear scale).

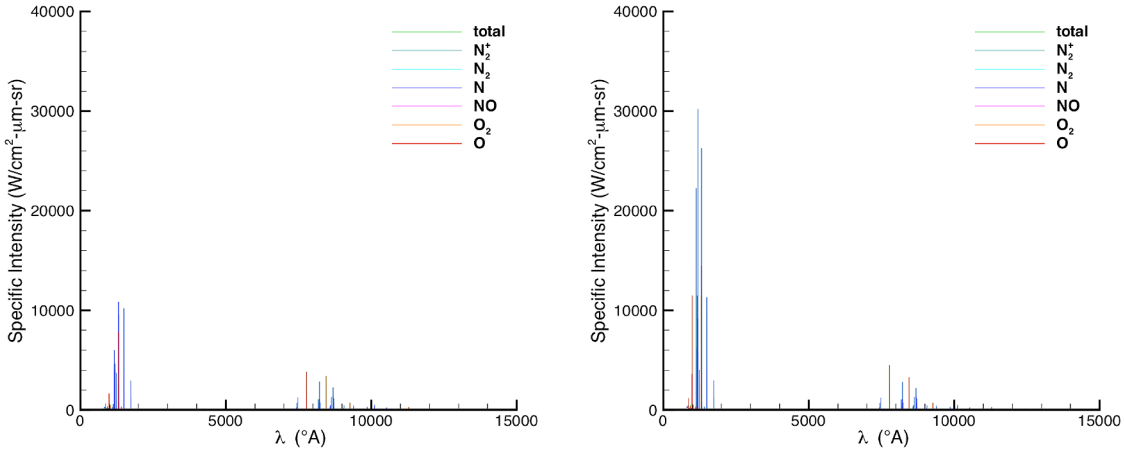

a) Inward **b) Outward**

Fig. 14 Stagnation point specific intensity spectra by species using model 12EQ (linear scale).

vibration temperatures, we find that the flow is still in thermal nonequilibrium in almost the entire shock-layer region at $t = 42$ s. However, the postshock thermochemical nonequilibrium flow does relax to thermal equilibrium at $t = 51$ s.

Figures 7a and 7b show the surface temperature distributions. Again, the ground state thermodynamics model shows higher surface temperatures than the excited-state thermodynamics model, approximately 90–150 K in the forebody. In the backshell, all three models produced the same surface temperature. At the peak-heating point, $t = 51$ s, the surface temperature is about 250 K higher than that at the earlier time at $t = 42$ s. Note that the current CFD model does not account for the ablation and heat conduction to the body; therefore, all predicted surface temperatures are several hundred degrees higher than the observations [22].

Figures 8–10 show the species number densities along the stagnation line, using the three models, respectively. The 17-species model seems to make the oxygen and nitrogen dissociation slightly faster than the 11- or 12-species models. The excited-state

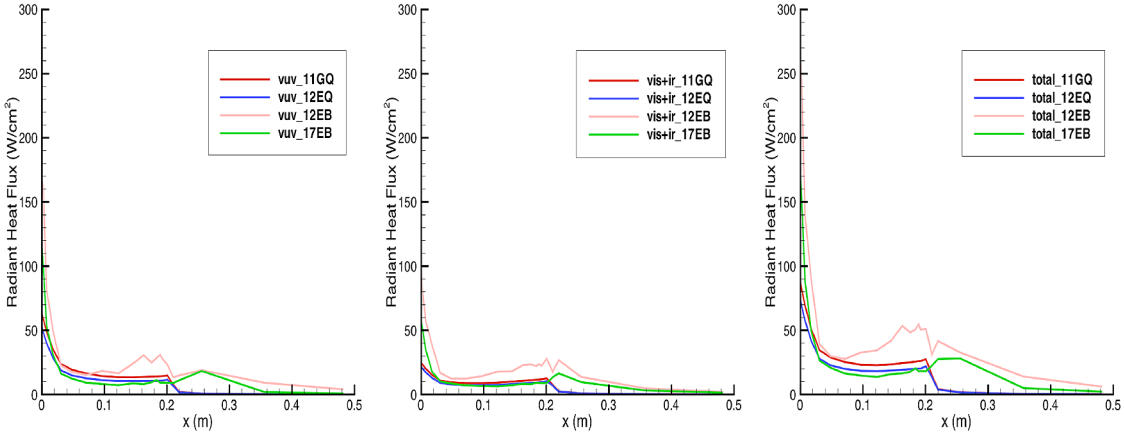

a) VUV **b) Vis+IR** **c) Total**

Fig. 15 Radiative heat flux to the body surface at $t = 51$ s, $z = 61.76$ km.

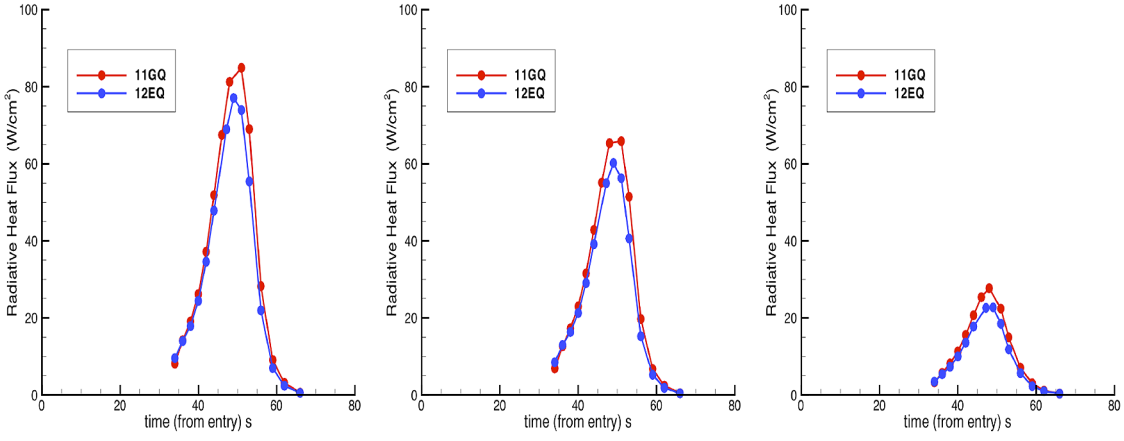

a) Stagnation point **b) Core 1** **c) Core 2**

Fig. 16 Estimated radiative heat flux history.

Table 4 Gaussian function FWHM

λ, nm	FWHM, Å
700–750	6.5
750–800	7.0
800–850	7.5
850–900	8.0

thermodynamics model generates a little more nitrogen and oxygen atoms but fewer electrons than those from the ground state thermodynamic model in the postshock region.

B. Radiative Heat Flux to Body Surface

As mentioned previously, the radiation simulations were carried out with the NEQAIR code, using the converged flow solutions from DPLR. The tangent-slab approximation is used here to predict the radiative heat flux to the body surface. We first constructed the normal lines of sight, as shown in Fig. 2, from a set of 21 points on the body surface. Each line of sight contains 65 radial points. Since the shock layer is so thin, increasing the number of radial points would not change the accuracy of the solution, even though only a first-order-accurate quadrature is used in the integration of the RTE. We have also used 129 points on each line of sight for some cases, and the answers are essentially the same. The translational and vibrational temperatures and species number densities at each radial point are interpolated from the flow solutions, using trilinear interpolation within the enclosing grid cell. Note that the free electron temperature is assumed to be the same as the heavy particle translational temperature in the flow calculation. However, in a nonequilibrium environment, due to the large difference in mass, the kinetic energy exchange between the electron and heavy particles is actually a very slowly equilibrating process. The QSS model assumes the electronic state excitation is mainly caused by electron impact collisions. If the electron temperature was set to the heavy particle temperature in that model, the predicted radiative heat flux would have been much too high. Therefore, we set the free electron temperature to be the same as the electronic temperature (or vibrational temperature) in the radiation calculation. This inconsistency between the flow and radiation fields will introduce some differences in the predicted radiative heat flux levels. However, the effect remains to be investigated.

We first present some results for the peak-heating case at $t = 51$ s. Figures 11 and 12 show both inward and outward (without blackbody radiation) specific intensity spectra by species on a logarithmic scale for the line of sight at the stagnation point, using the QSS radiation model with 11G and 12E (denoted as 11GQ and 12EQ in the figures), respectively. Similar plots on a linear scale are shown in Figs. 13 and 14. One immediately finds that almost all the radiation contribution comes from the atomic species O and N. This is most evident from the linear plots in Figs. 13 or 14. A comparison of the inward and outward spectra in the visible (VIS) and near infrared (IR) range (VIS plus IR, $200 \leq \lambda \leq 1400$ nm) shows no significant differences, implying that the gas is transparent, with very little absorption in this wavelength region. However, in the vacuum ultraviolet region (VUV) ($\lambda \leq 200$ nm), as shown clearly in Figs. 13 and 14, the specific intensity is much stronger for the outward case, indicating that there is some absorption in the boundary layer for the inward case in that spectral range.

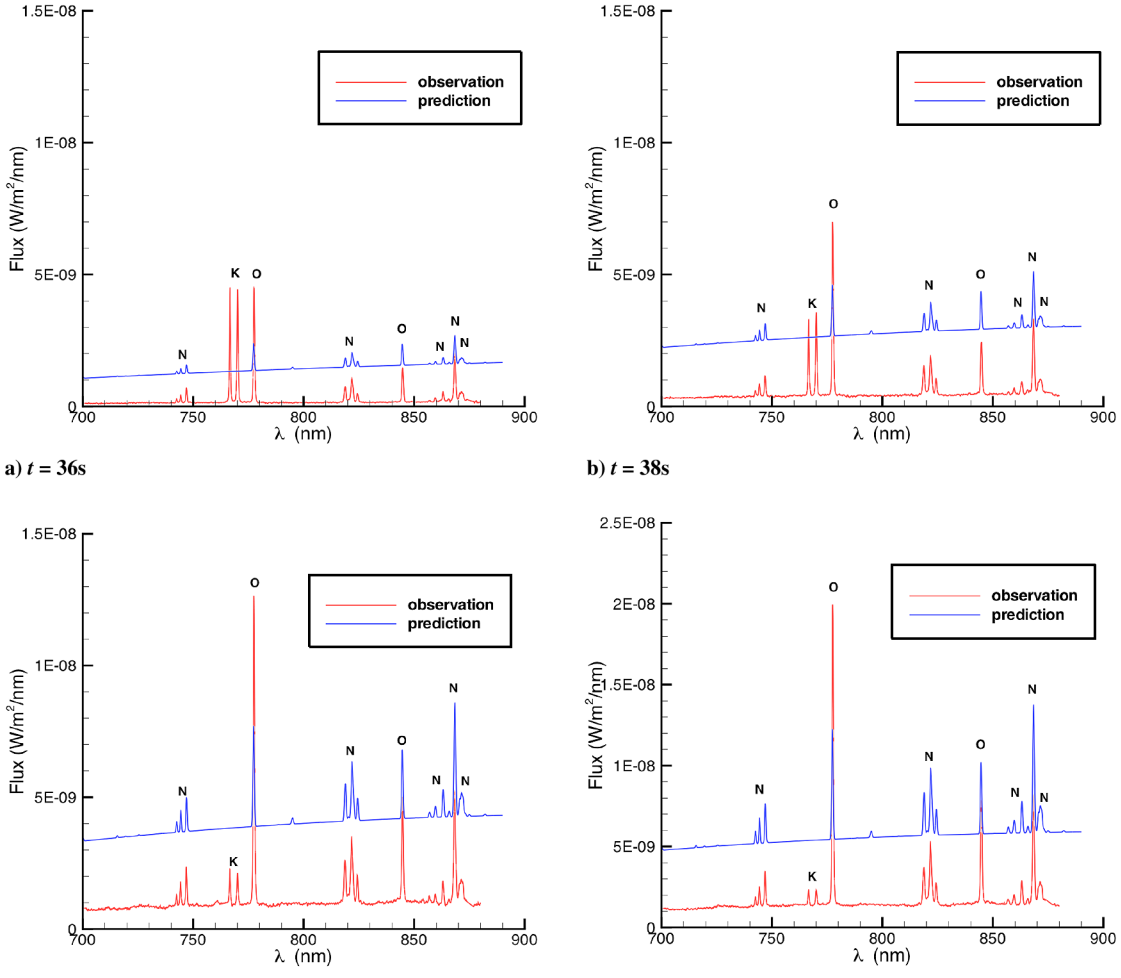

Fig. 17 Comparison of simulation results with ECHELLE spectra at various trajectory points.

In addition to the two models mentioned previously, we also employed the Boltzmann radiation model for the 12- and 17-species calculations (denoted as 12EB and 17EB). The radiative heat fluxes in the VUV and VIS-plus-IR regions and the total flux along the body, using the four models, are shown in Figs. 15a–15c, in which the distributed radiative heat fluxes are plotted as functions of the axial coordinate (x). The Boltzmann model gives too-strong radiation when compared with the QSS model. Furthermore, the bumps and kinks in the curves for both 12EB and 17EB near the shoulder region do not appear to be physical. Either the flowfield computed using CFD is not as smooth as one would expect (in a decoupled computation, radiation predictions reflect the smoothness of the underlying flow solution), or the Boltzmann model might not be a good choice at this trajectory point (the freestream density is quite small, and the vehicle scale is also quite small). We also see that the radiative heat flux is dominated by the contribution from the VUV region: about 70% of the total flux at the stagnation point. To provide information for the postflight TPS material analysis, we also computed the radiative heat flux history at three locations on the body at the stagnation ($x = 0.0$ m), core 1 ($x = 0.0087$ m), and core 2 ($x = 0.1026$ m) points. The history is shown on Fig. 16.

C. Simulation and Observation Data Comparison

To assess the current flow and radiation models used in nonequilibrium atmospheric entry simulations, we compared our predictions with observations. Here, we use data from the echelle-based spectrograph for the crisp and high efficient detection of low light emission (ECHELLE) instrument [7] for this comparison. The data were obtained during the time interval from $t = 33.8$ s to $t = 43.7$ s, when the radiative heating was most important. This covers the period of time when the DC-8 airborne observatory was at an altitude of $z = 11.89$ km and the SRC descended from an altitude of $z = 81$ km to $z = 69$ km. A total of 100 frames were recorded at every tenth of a second, covering the wavelength range of 370 to 880 nm at 0.14–0.9 nm resolution. The emission is not spatially resolved. At a given time, an ECHELLE spectrum is a measure of radiation emitted from the entirety of the glowing shock layer and body surface.

The data contain a broadband continuum, presumably from the hot heat-shield surface, shock-layer air plasma emissions of N, O, and N_2^+, as well as atomic hydrogen and CN molecular band emission from the ablating heat-shield material PICA and, early in the flight, atomic lines of Zn, K, Ca^+, Ca, and Na from a Z-93P paint applied to the top of the PICA. Since the present analysis is based on nonablating simulations, our comparisons are focused on the atomic nitrogen and oxygen lines in the wavelength range of 700 to 880 nm. Data reduced from the echelle spectrograph have been corrected for instrumental response, aircraft window transmission, and atmospheric extinction. The measured flux in each frame has an uncertainty generally within ±20%. Because of the level of noise in the measured data from frame to frame, we use 1 s time-averaged data to compare with our predictions.

The simulations involve spectral line-by-line computations at $t = 36, 38, 40, 42$ s, using the baseline model 11GQ. In addition, at $t = 42$ s, we also use the models 12EQ, 12EB, and 17EB. To have a meaningful and accurate comparison, we employed the full angular integration, as described in Sec. II.E. Here, we use a grid with 0.05×0.05 m resolution in the backplane. This gives approximately 200 lines of sight emitted from the body surface and 420 lines of sight

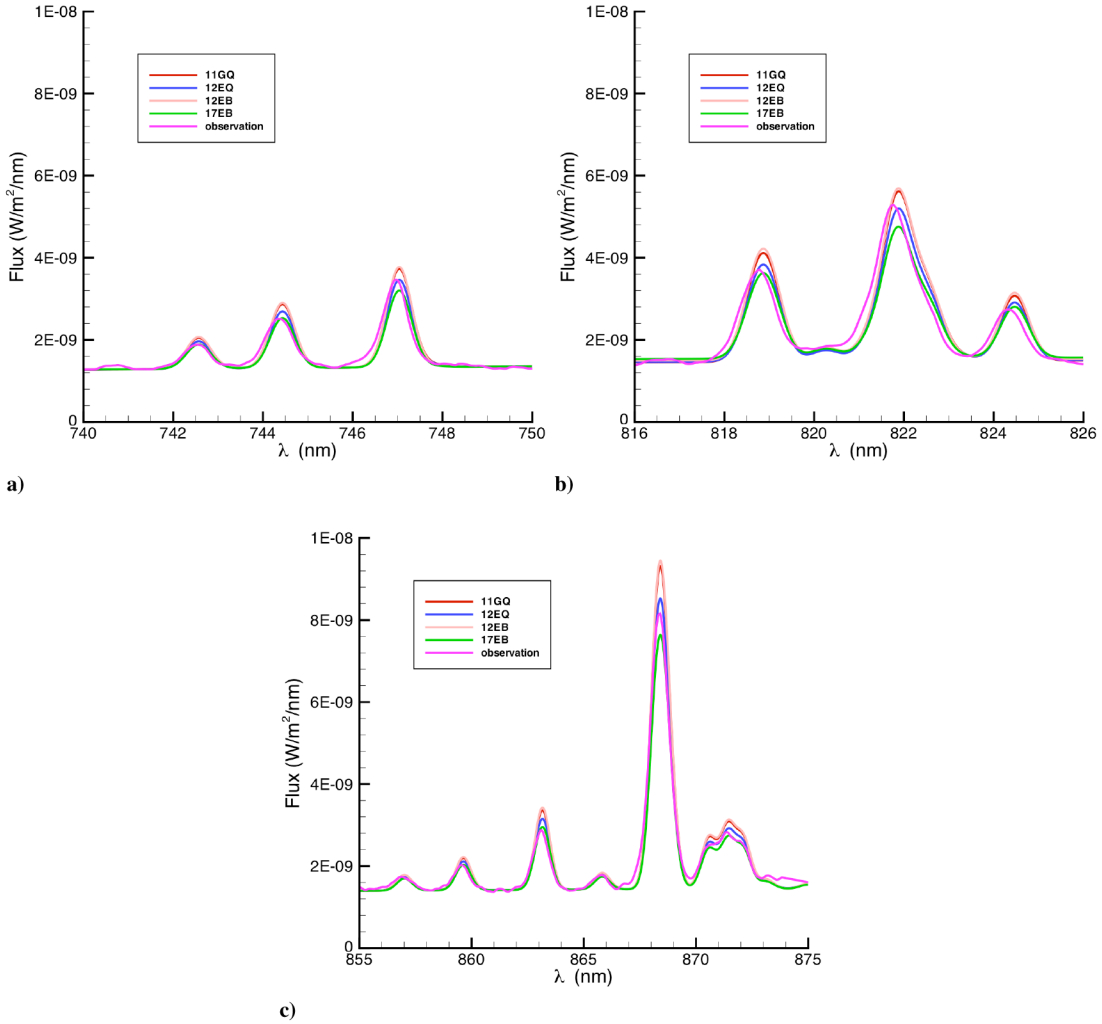

Fig. 18 Comparison of predicted atomic nitrogen lines with ECHELLE spectra at $t = 42$ s, $z = 71.19$ km.

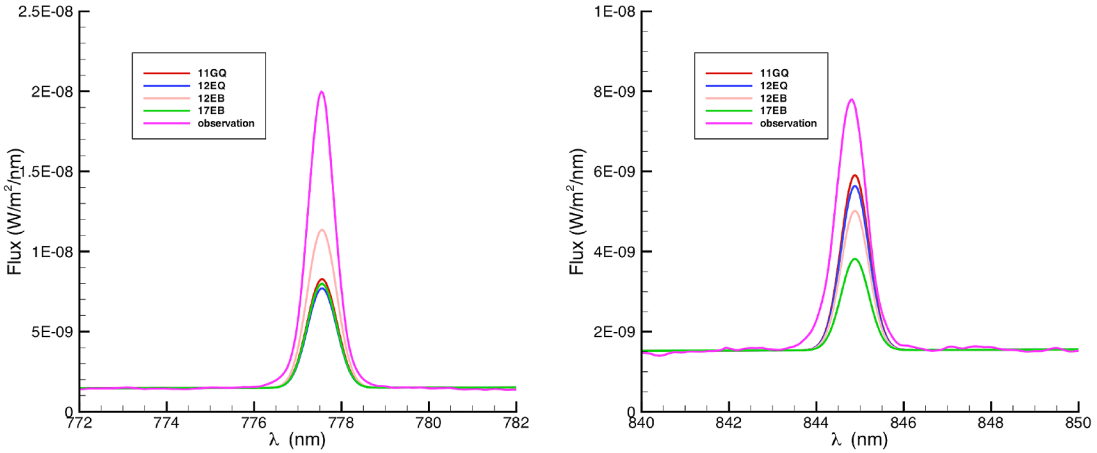

a) b)

Fig. 19 Comparison of predicted atomic oxygen lines with ECHELLE spectra at $t = 42$ s, $z = 71.19$ km.

from the surrounding shock layer. Because of the symmetry, only one-half of these lines of sight are needed for the computations. Our calculations include the blackbody radiation from the body surface but not reflections from the body or radiation scattering. To account for the ECHELLE camera responses [7] to the radiation, the NEQAIR results are convolved with Gaussian functions. Table 4 presents the full width at half maximum (FWHM) of each Gaussian function we used for four wavelength ranges.

Figures 17a–17d show comparisons of our simulations with the ECHELLE spectra at the four trajectory points. We note that the continuum (blackbody radiation) predictions are several times higher than the observation. As mentioned previously, this is due to the fact that we have not accounted for the ablation and heat conduction to the body in the CFD computations. The inclusion of the blackbody radiation here is only to check the shock-layer absorption.

Despite the difference in the continuum predictions, line strength (height above the continuum) matches the observation well for atomic N lines at all four trajectory points. However, this is not the case for the atomic O lines, for which we underestimate the strength. If we bring down the continuum predictions to the level of observations, we can directly compare our results with the observations. Figures 18 and 19 show the comparisons of our results of the four models with the ECHELLE spectra for nitrogen and oxygen lines, respectively, at $t = 42$ s. For the nitrogen lines, the 12EQ provides the closest prediction to the observation. As expected, the ground state thermodynamic model gives the highest prediction. The figures also show that the Boltzmann models make only a slightly higher prediction than that from the QSS model. Regardless of the small differences, all four models compare well with the observation.

For oxygen lines, all our models, including the Boltzmann model, underpredict the line strength. One possibility of this underprediction is due to uncertainty in the Einstein coefficients. The most recent compilation of data in the National Institute of Standards and Technology atomic spectra database** indicates the Einstein coefficients used in NEQAIR are too small for some of the oxygen lines. The new data show a 9% increase from 3.40×10^7 s^{-1} to 3.69×10^7 s^{-1} for the 777 nm line and a 15% increase from 2.80×10^7 s^{-1} to 3.22×10^7 s^{-1} for the 844.6 nm line. Since the gas is almost transparent in the VIS-plus-IR region, the amount of increase in the Einstein coefficient will give a similar amount of increase in the predicted line intensity. The other possibility is that the predicted populations of the upper energy states are too low (i.e., the collisional process of electron impact excitation in the QSS model is not as efficient). As indicated in the flow simulation, the flow at this time or altitude is still in thermal nonequilibrium, but the molecules are almost completely dissociated in the postshock region. Yet another possibility is ablation products, which are not currently included in our simulations. It is possible that additional atomic O from phenolic pyrolysis will contribute to strengthening the predicted line intensities. (PICA is made of phenolic resin, C_6H_5OH, which is a chemical compound consisting of carbon, hydrogen, and oxygen, but no nitrogen.) Clearly, further investigation is necessary to understand why the O lines are underpredicted.

**Data available online at http://physics.nist.gov/asd3 [retrieved 19 May 2009].

IV. Conclusions

A framework has been developed for computing the trajectory-based emission signature from the shock layer of an atmospheric entry spacecraft, and it has been applied to the Stardust capsule reentry at several points along its postflight BET. Despite the fact that the small size of the Stardust capsule spacecraft effectively makes it a point source at large observation distances, the framework creates a three-dimensional bounding box (depending on the view angle of the observer) around the capsule. This box includes the shock layer (and wake) and, thus, accounts for nonuniform distributions of both temperatures and species number densities in the near-body region. Using a uniform background Cartesian mesh, lines of sight from the body to the outer boundary are constructed in the direction of the observer. The RTE is then integrated along each LOS, using NEQAIR. The intensity at the first point on each LOS is that of a blackbody at the local radiation equilibrium temperature predicted by the flow solver. The emission (and absorption) was computed with high spectral resolution for select line and band systems of constituent atomic and molecular species.

Although the baseline physical model used in the flowfield computations is 11-species air without any excited electronic states in thermodynamics, numerous other experiments have been attempted, with inclusion of excited electronic states and additional species (atmospheric argon and carbon dioxide). Furthermore, two different methods are considered for populating excited electronic states in radiation computations: a (multitemperature) Boltzmann distribution model and a model based on excitation due to electron impact (QSS). For each variation, the computed synthetic spectra are convolved with the instrument function of the echelle spectrograph, and comparisons are made between predictions and calibrated measurements.

Overall, the predictive tools replicate the general features and trends in the measured spectra. Since the flow model does not include either potassium or zinc (major components of the zinc oxide-based white paint used on the heat shield), the synthetic spectra do not contain these lines in the predicted emission signatures. One obvious difference is in the levels of the background continuum. This is due to the surface temperature from the computed flow solution; flow computations without inclusion of material thermal response will result in higher surface temperatures. Working with base-to-peak ratios (in both experiment and computations) for individual atomic lines, the level of agreement for atomic N lines is good. However, the

level of agreement for atomic O lines is poor, even for the case of a (multitemperature) Boltzmann distribution. Clearly, the population levels of O in the excited electronic states are lower than expected. This suggests that the excitation model for populating electronic levels of the O atom needs to be examined a little more closely.

The present paper is a report on the status of work accomplished thus far, with small changes to the predictive tools and methods. More investigations are underway to explain the discrepancies between experiment and prediction, especially in electron impact excitation rates. Furthermore, inclusion of ablation products in the gas phase is also being pursued to investigate the CN radiation.

Acknowledgments

This work was funded and managed by the Hypersonics Project in the Fundamental Aeronautics Program, Orion Thermal Protection System Advanced Development Project, and the NASA Engineering and Safety Center. The ELORET Corporation's contributions to this work were performed under NASA Ames Research Center contract NNA04BC25C. NASA's DC-8 airborne laboratory was deployed by the University of North Dakota/ National Suborbital Education and Research Center, under contract with NASA Wallops Flight Center, in a project initiated and coordinated by the SETI Institute.

References

[1] Olynik, D., Chen, Y. K., and Tauber, M., "Aerothermodynamics of the Stardust Sample Return Capsule," *Journal of Spacecraft and Rockets*, Vol. 36, No. 3, 1999, pp. 442–462. doi:10.2514/2.3466

[2] Park, C., "Calculation of Stagnation-Point Heating Rates Associated With Stardust Vehicle," *Journal of Spacecraft and Rockets*, Vol. 44, No. 1, 2007, pp. 24–32. doi:10.2514/1.15745

[3] Desai, P., Qualls, G., and Levit, C., "Stardust Entry Reconstruction," AIAA Paper 2008-1198, Jan. 2008.

[4] Levit, C., Albers, J., Jenniskens, P., and Spurny, P., "Reconstruction and Verification of the Stardust SRC Reentry Trajectory," AIAA Paper 2008-1199, Jan. 2008.

[5] Whiting, E. E., Park, C., Liu, Y., Arnold, J. O., and Paterson, J. A., "NEQAIR96, Nonequilibrium and Equilibrium Radiative Transport and Spectra Program: User's Manual," NASA Rept. 1389, Dec. 1996.

[6] Wright, M. J., Candler, G. V., and Bose, D., "Data-Parallel Line Relaxation Method for the Navier–Stokes Equations," *AIAA Journal*, Vol. 36, No. 9, 1998, pp. 1603–1609. doi:10.2514/2.586

[7] Jenniskens, P., "Observations of the STARDUST Sample Return Capsule Entry with a Slit-Less Echelle Spectrograph," 46th AIAA Aerospace Sciences Meeting and Exhibit, AIAA Paper 2008-1210, 2008.

[8] Hartung-Chambers, L., "Predicting Radiative Heat Transfer in Thermochemical Nonequilibrium Flow Fields, Theory and User's Manual for the LORAN Code," NASA TM 4564, Sept. 1994.

[9] Wright, M. J., Bose, D., and Olejniczak, J., "The Impact of Flowfield-Radiation Coupling on Aeroheating for Titan Aerocapture," *Journal of Thermophysics and Heat Transfer*, Vol. 19, No. 1, Jan. 2005, pp. 17–27. doi:10.2514/1.10304

[10] Wright, M. J., Bose, D., Palmer, G. E., and Levin, E., "Recommended Collision Integrals for Transport Property Computation, Part 1, Air Species," *AIAA Journal*, Vol. 43, No. 12, 2005, pp. 2558–2564. doi:10.2514/1.16713

[11] Wright, M. J., Hwang, H. H., Schwenke, D. W., "Recommended Collision Integrals for Transport Property Computation, Part 2, Mars and Venus Entries," *AIAA Journal*, Vol. 45, No. 1, 2007, pp. 281–288. doi:10.2514/1.24523

[12] Gupta, R. N., Yos, J. M., Thompson, R. A., and Lee, K., "A Review of Reaction Rates and Thermodynamic and Transport Properties for an 11-Species Air Model for Chemical and Thermal Nonequilibrium Calculations to 30,000 K," NASA Rept. 1232, Aug. 1990.

[13] Bartlett, E. P., Kendal, R. M., and Rindal, R. A., "An Analysis of the Coupled Chemically Reacting Boundary Layer and Charring Ablator: Part 4: A Unified Approximation for Mixture Transport Properties for Multi-Component Boundary-Layer Applications," NASA CR 1063, June 1968.

[14] Ramshaw, J. D., "Self-Consistent Effective Binary Diffusion in Multicomponent Gas Mixtures," *Journal of Non-Equilibrium Thermodynamics*, Vol. 15, No. 3, 1990, pp. 295–300. doi:10.1515/jnet.1990.15.3.295

[15] Park, C., *Nonequilibrium Hypersonic Aerothermodynamics*, Wiley, New York, 1990.

[16] Park, C., Howe, J. T., Jaffe, R. J., and Candler, G. V., "Review of Chemical-Kinetic Problems of Future NASA Missions, II: Mars Entries," *Journal of Thermophysics and Heat Transfer*, Vol. 8, No. 1, Jan. 1994, pp. 9–23. doi:10.2514/3.496

[17] Gessman, R. J., Laux, C. O., and Kurger, C. H., "Experimental Study of Kinetic Mechanisms of Recombining Atmospheric Pressure Air Plasma," AIAA Paper 1997-2364, June 1997.

[18] Millikan, R., and White, D., "Systematics of Vibrational Relaxation," *Journal of Chemical Physics*, Vol. 39, No. 12, 1963, pp. 3209–3213. doi:10.1063/1.1734182

[19] Cornette, E. S., "Forebody Temperatures and Calorimeter Heating Rates Measured During Project Fire II Reentry at 11.35 Kilometers per Second," NASA TM X-1305, Nov. 1966.

[20] Liu, Y., Prabhu, D., Saunders, D., Vinokur, M., and Dateo, C., "Comparison of Tangent Slab Approximation and Full Angular Integration in C'omputing Radiative Heating for the CEV Heatshield," NASA TN EG-CAP-06-124, Aug. 2006.

[21] Ozawa, T., Zhong, J., Levin, D. A., Boger, D., and Wright, M., "Modeling of the Stardust Reentry Flow with Ionization in DSMC," AIAA Paper 2007-611, Jan. 2007.

[22] Trumble, K. A., Cozmuta, I., Sepka, S., and Jenniskens, P., "Post-Flight Aerothermal Analysis of the Stardust Sample Return Capsule," AIAA Paper 2008-1201, Jan. 2008.

M. Wright
Guest Editor